RSC Advances

PAPER

View Article Online
View Journal | View Issue

Check for updates

Cite this: *RSC Adv.*, 2018, **8**, 15358

Facile synthesis of porous Fe_3O_4@C core/shell nanorod/graphene for improving microwave absorption properties†

Chen Fu, Dawei He,* Yongsheng Wang and Xuan Zhao

Received 2nd March 2018
Accepted 11th April 2018

DOI: 10.1039/c8ra01838c

rsc.li/rsc-advances

Porous Fe_3O_4@C core/shell nanorods decorated with reduced graphene oxide (RGO) were fabricated through a facile one-pot method. The microwave absorption properties of the samples can be adjusted by the weight ratio of RGO. The addition of RGO not only effectively reduces the agglomeration of Fe_3O_4@C, but also has a great effect on impedance matching and dielectric loss, resulting in enhanced microwave absorption abilities. The thickness corresponding to optimum reflection loss (R_L) decreases as the weight ratio of RGO increases. For the Fe_3O_4@C/RGO composite, a maximum R_L value of −48.6 dB can be obtained at 13.9 GHz with a thickness of 3.0 mm, and the absorption bandwidth with R_L below −10 dB is 7.1 GHz from 10.9 GHz to 18 GHz. These results demonstrate a facile method to prepare a highly efficient microwave absorption material with special microstructure.

Open Access Article. Published on 24 April 2018. Downloaded on 12/19/2024 5:44:11 AM.
This article is licensed under a Creative Commons Attribution-NonCommercial 3.0 Unported Licence.

1. Introduction

More and more microwave radiation is generated through the development of science and technology, causing pollution to the environment and cause harm to human beings. So over the past few years, tremendous research efforts have been focused on the fabrication of microwave absorption materials.[1–4] According to absorption mechanism,[5] traditional microwave absorption materials can classified into magnetic loss materials such as ferrite[6] and magnetic metal powders,[7] and dielectric loss materials such as metal oxides,[8] carbon materials[9] and conduction polymers.[10] Compared with conductive loss materials, magnetic loss materials have a high density and a narrow bandwidth.[11] It is efficient to combine magnetic loss materials with conductive loss materials in order to enhance microwave absorption ability.[5]

As a traditional microwave absorption material, Fe_3O_4 has great potential due to its strong absorption properties and low cost.[12] However, its high density and narrow absorption frequency bandwidth limit the application of pure Fe_3O_4 material.[13] For a magnetic material Fe_3O_4 has a relatively small permittivity, which limits its widespread use in the microwave absorption field.[14] Meanwhile, the microwave absorption properties of absorbers also depend on their size, structure and morphology.[15] Therefore various Fe_3O_4 of different structures, and its composites combined with ZnO,[16] polyaniline,[13] graphene,[17,18] and other dielectric materials,[19,20] have been explored to improve the balance between permittivity and permeability. Liu *et al.* synthesized heterostructured nanorings of Fe_3O_4@C and Fe_3O_4/Fe@C, which show enhanced absorption properties and absorption bandwidth.[21] Sun *et al.* obtained hierarchical dendrite-like materials of Fe_3O_4, γ-Fe_2O_3 and Fe with excellent microwave absorption ability at low or middle frequency.[22] Core–shell Fe_3O_4@C composites with different thicknesses of the carbon shell were prepared and the relationship between absorption ability and thickness of the carbon shell was explored according to Du's work.[23]

Because of high surface areas, low density and carrier mobilities coupled with abundant defects and hydroxyl, epoxy, and carboxyl groups, reduced graphene oxide (RGO) has received much attention in the microwave absorption field.[24] Pristine RGO has unsatisfactory microwave absorption because of agglomeration effects and a permittivity that is too high, which is disadvantage to impedance matching.[25] On the other hand, due to its special microstructure RGO can serve as a template for the growth of metal oxide nanoparticles and polymers. Therefore, decorating RGO with magnetic and dielectric materials such as ZnO,[26] Fe_3O_4,[27] Co_3O_4,[28] MnO_2,[29] $NiFe_2O_4$,[30] and polyaniline,[31] is an effective method to solve the problem of impedance matching, and it can also prevent the aggregation of nanoparticles. Ren *et al.* fabricated a 3D SiO_2@Fe_3O_4 core/shell nanorod array/graphene composite with a maximum R_L of −31.9 dB.[19]

The aim of this work was to synthesize core/shell nanostructures using GO as the template. Herein, porous Fe_3O_4@C core/shell nanorods decorated with reduced graphene oxide were synthesized by a facile one-pot method. We also explored the microwave absorption properties of Fe_3O_4@C/RGO for

Key Laboratory of Luminescence and Optical Information, Ministry of Education, Institute of Optoelectronic Technology, Beijing Jiaotong University, Beijing 100044, China. E-mail: dwhe@bjtu.edu.cn; Tel: +86 10 51688018

† Electronic supplementary information (ESI) available. See DOI: 10.1039/c8ra01838c

This journal is © The Royal Society of Chemistry 2018

Open Access Article. Published on 24 April 2018. Downloaded on 12/19/2024 5:44:11 AM.
This article is licensed under a Creative Commons Attribution-NonCommercial 3.0 Unported Licence.

different weight ratios of RGO. The experimental results show that this composite has an enhanced microwave absorption ability with strong absorption (maximum reflection loss of −48.6 dB), small thickness (3.0 mm), and a broad effective absorption bandwidth (7.1 GHz) when R_L < 10 dB. The results indicate that porous Fe_3O_4@C core/shell nanorod/RGO prepared though this facile method, which possesses excellent microwave absorption ability, is an ideal candidate for microwave absorbers.

2. Experimental

All chemicals were obtained from Alfa Aesar and used without further purification except the aniline monomer. The aniline monomer was purified by distillation under the protection of high purity N_2 before use. Graphene oxide (GO) was prepared through a modified Hummer's method.[4] Deionized water was prepared by Aquapro EDI2-3002-U.

2.1 Synthesis of porous Fe_3O_4@C core/shell nanorod

0.8 g $FeCl_3 \cdot 6H_2O$, 1.8 g urea and different concentrations of glucose (0.1, 0.2, 0.3 M) were added into 30 ml DI H_2O and stirred for 1 hour to ensure full dispersion. The resultant solution was transferred into a 100 ml Teflon-lined stainless steel autoclave and kept at 180 °C for 8 h. The black solution was centrifuged and washed with ethanol and DI H_2O, and then dried by vacuum cryogenic desiccation for 12 h. At last, the powders were sintered at the temperature of 400 °C for 1 h under Ar atmosphere. The synthesis method of pure Fe_3O_4 was the same as for Fe_3O_4@C, but without glucose.

2.2 Synthesis of porous Fe_3O_4@C core/shell nanorod/graphene (Fe_3O_4@C/RGO)

A certain amount of GO powder was dispersed in 30 ml DI H_2O and stirred for 12 hours under strong magnetic stirring, followed by sonication for 4 hours to obtain a GO suspension of differing concentrations (0.2, 0.4, 0.8, 1.2 mg ml^{-1}). 0.8 g $FeCl_3 \cdot 6H_2O$, 1.8 g urea and 1 g glucose were added into the GO solution and stirred for 1 hour to obtain a clear solution. The resultant solution was transferred into a 100 ml Teflon-lined stainless steel autoclave and kept at 180 °C for 8 h. The black solution was centrifuged and washed with ethanol and DI H_2O, and then dried by vacuum cryogenic desiccation for 12 h. As was done for Fe_3O_4@C, the powders were also sintered at the temperature of 400 °C for 1 h under Ar atmosphere. The samples with different concentrations of RGO were named CFG1 (0.2 mg ml^{-1}), CFG2 (0.4 mg ml^{-1}), CFG3 (0.8 mg ml^{-1}) and CFG4 (1.2 mg ml^{-1}).

2.3 Measurements

The morphology of the products was observed by transmission electron microscopy (TEM: 1200EX, JEM) and a high-resolution transmission electron microscope (HRTEM: Tecnai G2 F20 S-TWIN, FEI). The structural and elemental characterization of the samples was carried out by powder X-ray diffraction (XRD: D8 Advance, Bruker) using Co Kα radiation, Raman spectroscopy (Renishaw inVia) and Thermogravimetric Analysis (TGA: TGA/DSC 1 SF/1382, METTLER). The magnetic properties were studied by a vibrating-sample magnetometer (ASM: Squid-VSM, Quantum Design). X-ray photoelectron spectra were obtained using an X-ray photoelectron spectrometer (XPS: Thermo ESCALAB 250XI, Thermo Electron Corporation).

The samples for electromagnetic parameter measurement were prepared by mixing paraffin with 40 wt% sample, which was pressed into toroidal shapes of 3 mm in inner diameter, 7 mm in outer diameter, and a thickness of 2 mm. The complex permittivity and complex permeability of the samples was characterized by a HP8722ES vector network analyzer in the frequency range 1–18 GHz. The reflection loss (R_L) is calculated according to the following equations:[32]

$$R_L = 20 \lg \left| \frac{Z_{in} - 1}{Z_{in} + 1} \right| \quad (1)$$

$$Z_{in} = \sqrt{\mu_r / \varepsilon_r} \tanh\left[j(2\pi f d / c) \sqrt{\mu_r \varepsilon_r} \right] \quad (2)$$

where Z_{in} is the input impedance, ε_r and μ_r are the relative complex permittivity and permeability respectively, f is the frequency of the microwaves, d is the layer thickness and c is the velocity of microwaves in free space.

3. Results and discussion

The morphologies of Fe_3O_4, Fe_3O_4@C and Fe_3O_4@C/RGO were investigated by TEM (Fig. 1 and S1†). As shown in Fig. 1a, the pure Fe_3O_4 nanorods are like needles 50–90 nm in size. Following the addition of glucose, Fe_3O_4@C has a porous structure. When the concentration of glucose is 0.1 M (Fig. S1b†), it exhibits no significant change compared with pure Fe_3O_4. Continuing the increase in concentration of glucose to 0.2 M (Fig. 1b and S1c†), a thin carbon film is coated on the Fe_3O_4 nanorod with a porous structure. From Fig. S1d,† when the concentration of glucose is larger than 0.3 M, the polymerization of more glucose will link Fe_3O_4@C together to form a film resulting in an aggregation phenomenon. In order to prevent the aggregation of Fe_3O_4@C, graphene was introduced into the synthetic system. As shown in Fig. 1c, Fe_3O_4@C growth on the surface of graphene sheets is relatively scattered compared with that for pure Fe_3O_4@C (Fig. 1c). More importantly, the HRTEM (Fig. 1d) shows a clear core/shell structure.

To further investigate the structure of Fe_3O_4@C, the samples were subjected to thermal treatments of different temperature under air atmosphere. In this process, the carbon atoms which are coated on Fe_3O_4 can react with oxygen in the air: $C + O_2 = CO_2$. Thus, pure and porous Fe_3O_4 nanorods without carbon could be obtained. In Fig. 2b, there is still a carbon film coating on the Fe_3O_4 nanorods following thermal treatment at the temperature of 300 °C. However, following thermal treatment at the temperature of 400 °C, the carbon atoms had reacted sufficiently. But with a further increase to the temperature of thermal treatment the structure of Fe_3O_4 breaks, which can be obviously seen in Fig. 2d.

The structure and magnetic properties of Fe_3O_4@C/RGO (CFG2) were investigated by XRD, Raman, TGA and using the

Open Access Article. Published on 24 April 2018. Downloaded on 12/19/2024 5:44:11 AM.
This article is licensed under a Creative Commons Attribution-NonCommercial 3.0 Unported Licence.

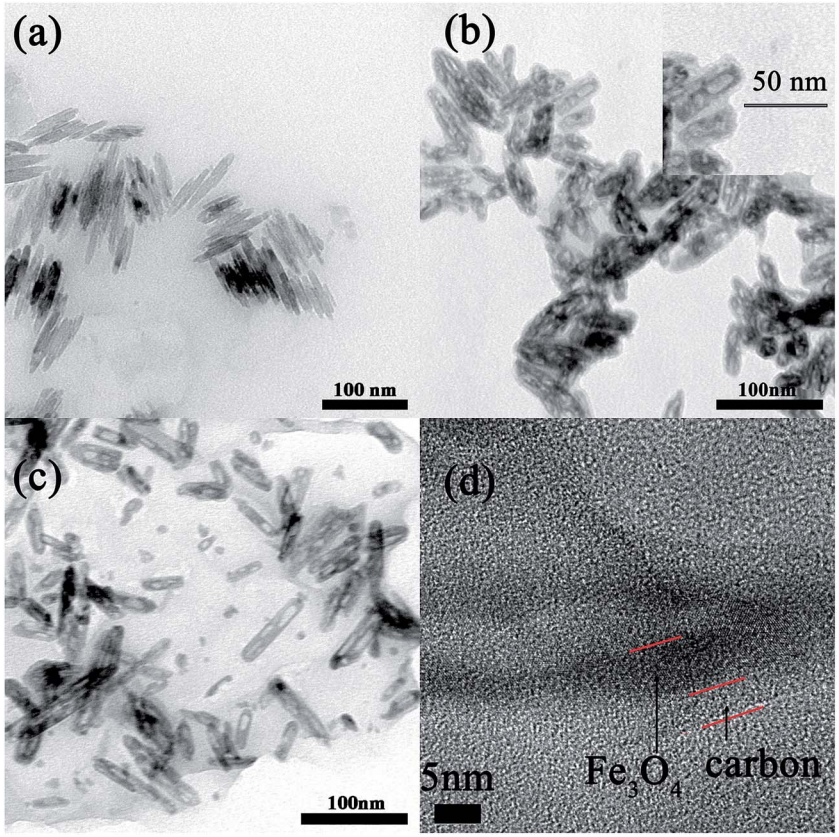

Fig. 1 TEM images of (a) Fe_3O_4 nanorods, (b) Fe_3O_4@C, (c) Fe_3O_4@C/RGO (CFG2), and (d) HRTEM of Fe_3O_4@C/RGO (CFG2).

magnetisation curve. Fig. 3a demonstrates the X-ray diffraction patterns of Fe_3O_4@C and Fe_3O_4@C/RGO. The diffraction peaks of Fe_3O_4@C are observed at $2\theta = 21.2°$, 35.1°, 41.4°, 50.4°, 62.9°, 67.2° and 74.2° corresponding to the (1 1 1), (2 2 0), (3 1 1), (4 0 0), (4 2 2), (5 1 1) and (4 4 0) reflections of Fe_3O_4, respectively. These peak values of Fe_3O_4 matched the standard XRD pattern (JCPDS no. 19-0629).[16] For Fe_3O_4@C/RGO, the main peaks of Fe_3O_4@C can be found which prove the successful synthesis of Fe_3O_4@C and the existence of RGO has no effect on the crystal structure of Fe_3O_4. In Fig. S2,† two lattice spacings can be seen which correspond to the (2 2 0) and (3 1 1) reflections of Fe_3O_4. The broad peak appearing at 30° is attributed to amorphous carbon.[33] In the Raman spectrum of Fe_3O_4@C/RGO (Fig. 3b) the D band at 1338.44 cm^{-1} and the G band at 1584.44 cm^{-1}, which correspond to defects or the edge and vibration of sp^2 hybridized carbon–carbon bonds, were observed.[12] The TGA pattern of Fe_3O_4@C/RGO shows two weight losses. The first slow decrease of the TG curve before 230 °C is attributed to the removal of residual functional groups on RGO.[34] The second is in the range 230–450 °C, and is due to the decomposition of RGO and other amorphous carbon. After 450 °C the TG curve remains stable, revealing the complete removal of RGO and amorphous carbon. For CFG2, the weight ratio of Fe_3O_4 is 36.5%. To understand the magnetic properties of Fe_3O_4@C/RGO, the room-temperature magnetic properties of CFG2 were examined with a magnetometer. As shown in Fig. 3d, significant hysteresis loops in the *M–H*

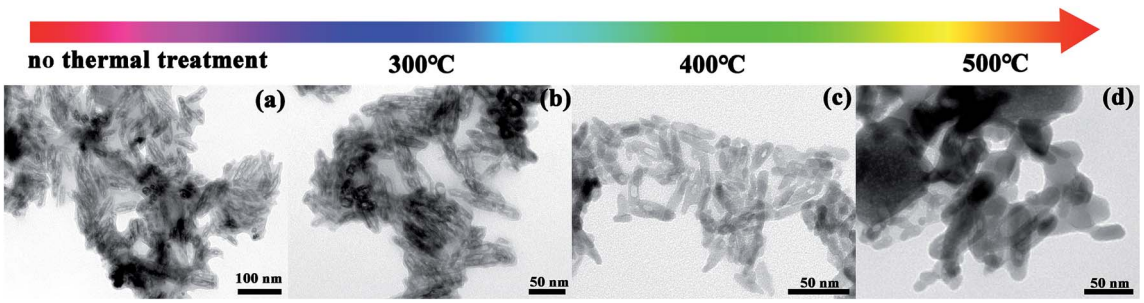

Fig. 2 TEM images of Fe_3O_4@C after thermal treatments at different temperatures.

This journal is © The Royal Society of Chemistry 2018

Open Access Article. Published on 24 April 2018. Downloaded on 12/19/2024 5:44:11 AM.
This article is licensed under a Creative Commons Attribution-NonCommercial 3.0 Unported Licence.

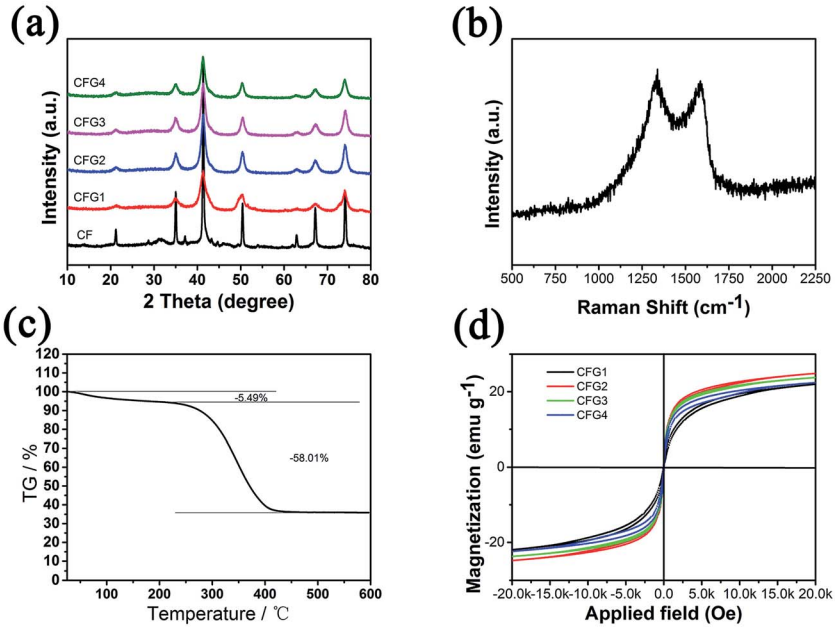

Fig. 3 (a) XRD pattern, (b) Raman spectrum, (c) TGA graph, and (d) magnetization curve of CFG, of Fe_3O_4@C.

curve are observed, indicating the ferromagnetic behavior of CFG2. The values of magnetization (M_s) for CFG1, CFG2, CFG3 and CFG4 are 22.0, 24.8, 23.8 and 22.4 emu g^{-1}, which are smaller than the corresponding bulk value (92 emu g^{-1})[35] due to the present of nonmagnetic graphene and amorphous carbon. The higher value of M_s for CFG2 can be attributed to the better dispersion of Fe_3O_4. The lower value of M_s of CFG3 and CFG4 is due to the increased weight of graphene which influences the M_s more than the dispersion.

The detailed elemental composition of CFG2 was characterized by XPS; the resulting spectra are shown in Fig. 4. In the full scan XPS spectrum (Fig. 4a), four sharp peaks with binding energies of 285, 399, 532 and 711 eV, were attributed to C 1s, N 1s, O 1s and Fe 2p, respectively; this result confirms the presence of C, N, O and Fe elements in the composite. Among these, the presence of N indicates the participation of urea in the synthetic process. For further investigation the electronic states of the elements were determined from the high-resolution spectra. In the C 1s spectrum (Fig. 4b) the fitted peaks with

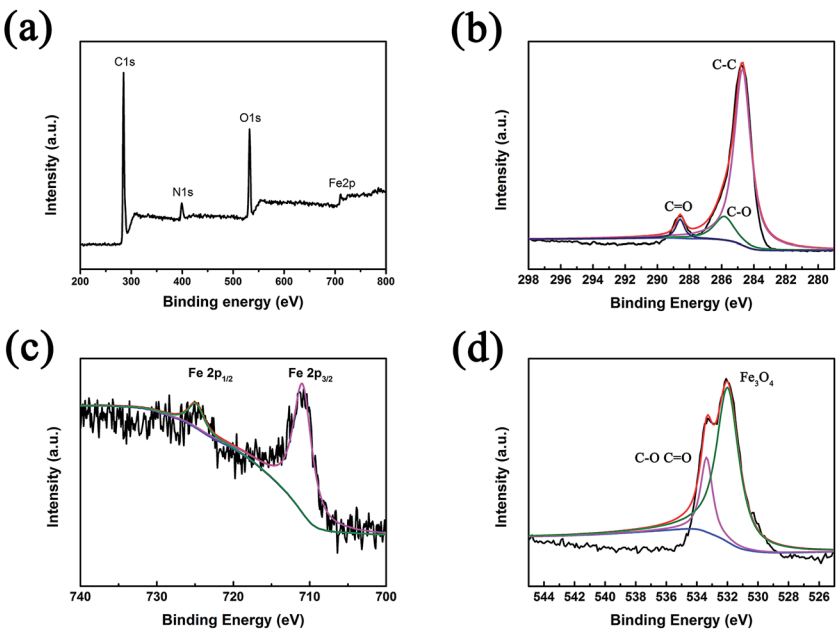

Fig. 4 XPS spectra of the CFG2 composite: (a) overview; (b), (c) and (d) are the high-resolution spectra of C, Fe, O, respectively.

Open Access Article. Published on 24 April 2018. Downloaded on 12/19/2024 5:44:11 AM.
This article is licensed under a Creative Commons Attribution-NonCommercial 3.0 Unported Licence.

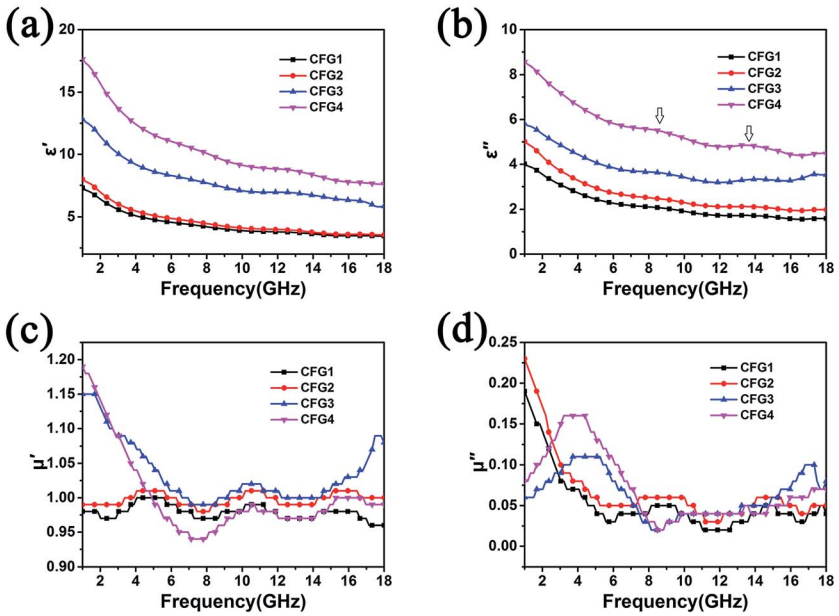

Fig. 5 The real part (a) and imaginary part (b) of the permittivity, and the real part (c) and imaginary part (d) of the permeability for Fe_3O_4@C/RGO composites with different compositions of RGO.

binding energy of 284.7, 285.9 and 288.6 eV can be attributed to C–C, C–O and C=O, respectively. Fig. 4c shows that the Fe 2p spectrum can be divided into two fitted peaks, corresponding to Fe $2p_{1/2}$ (725.1 eV) and Fe $2p_{3/2}$ (711.1 eV).[36] Two peaks are present at 533.4 eV and 532.0 eV in the high resolution spectrum of O 1s in Fig. 4d, which can be attributed to C–O/C=O and Fe_3O_4. The high-resolution spectrum of N shown in Fig. S3† demonstrates N doping in the composite. From the high-resolution XPS spectrum of N (Fig. S3†), three peaks corresponding to imine (–N=), amine (–NH–) and protonated amine ($-N^+-$) can be found. The XPS results further confirm the reduction of GO, during which the Fe_3O_4@C nanorods were formed on the surface of the graphene sheets.

To understand the possible microwave absorption mechanism, the relative complex permittivity and permeability of the Fe_3O_4@C and Fe_3O_4@C/RGO composites were investigated in the frequency range 1–18 GHz (Fig. 5 and S4†). Fig. 5a and b show the real (ε') and imaginary (ε'') parts of the relative complex permittivity ($\varepsilon_r = \varepsilon' - j\varepsilon''$) of the Fe_3O_4@C/RGO composites with differing compositions of RGO. The values of ε' and ε'' prominently increase compared with those of Fe_3O_4@C (Fig. S4a and b†). For Fe_3O_4@C/RGO composites, when increasing the content of GO, the value of ε' shows differing levels of improvement. For CFG1 and CFG2, ε' slightly increases. But, when further increasing the weight ratio of GO, the ε' values are obviously enhanced. This is due to a better conducting network, which can be formed when more GO is added into the materials system. The rise in the RGO weight ratio of Fe_3O_4@C/RGO composites benefits the increase in conductivity, resulting in strong dielectric loss. Two dielectric relaxation peaks can be found in the ε'' curve ranged from 6–16 GHz, which can be attributed to dipole polarization and interfacial polarization from the interface of Fe_3O_4 cores, C shells and RGO. Following an increase in the weight ratio of RGO the dielectric relaxation peaks are more notable, which proves that the aggregation of Fe_3O_4@C can be prevented by the addition of RGO, resulting in more contact interface with microwaves. The real (μ') and imaginary (μ'') parts of the relative complex

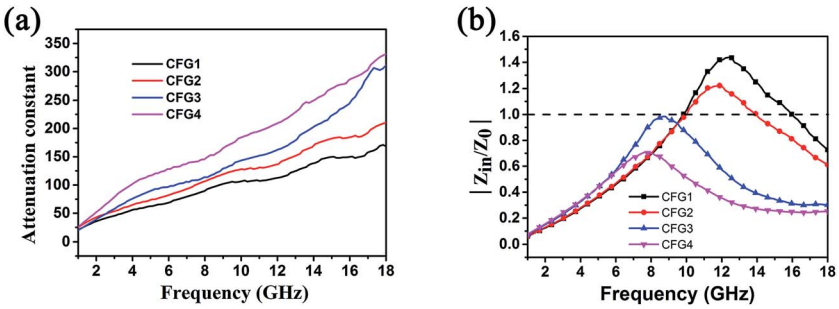

Fig. 6 (a) The attenuation constants of Fe_3O_4@C/RGO with different weight ratios of RGO, and (b) frequency dependencies of $|Z_{in}/Z_0|$.

 This journal is © The Royal Society of Chemistry 2018

Open Access Article. Published on 24 April 2018. Downloaded on 12/19/2024 5:44:11 AM.
This article is licensed under a Creative Commons Attribution-NonCommercial 3.0 Unported Licence.

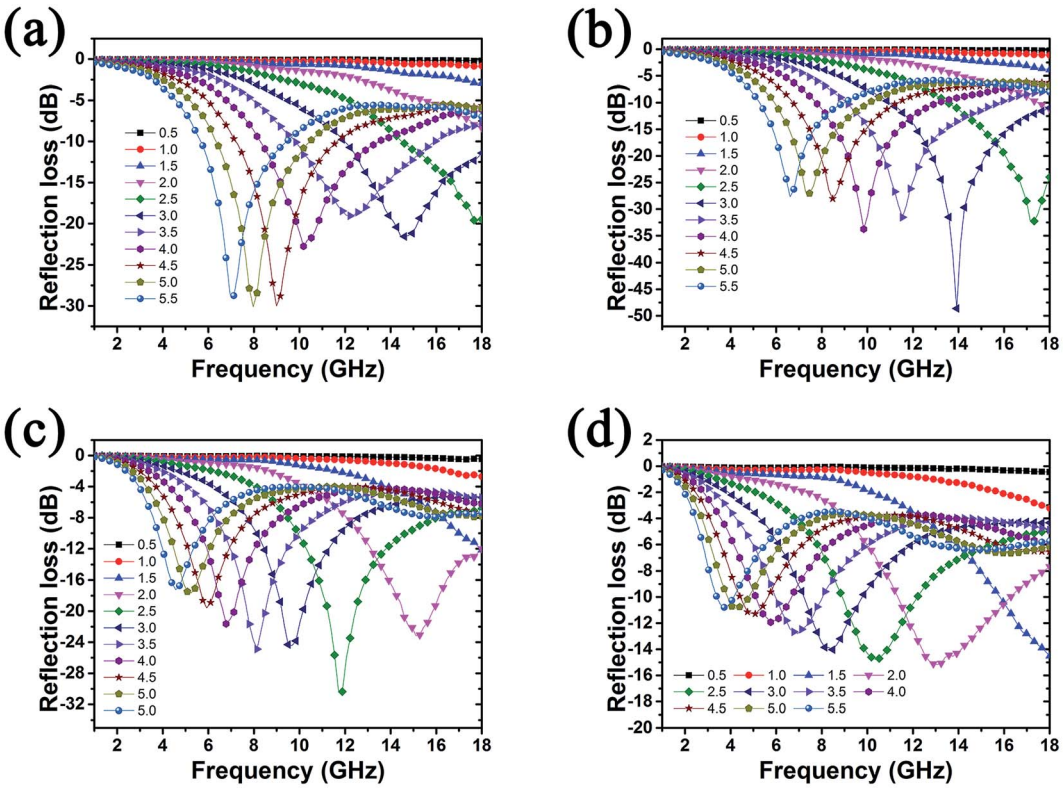

Fig. 7 Refection loss of Fe_3O_4@C/RGO composites with different weight ratios of graphene: (a) CFG1, (b) CFG2, (c) CFG3, and (d) CG4.

permeability are enhanced by the addition of RGO (Fig. S4c and d†) and Fe_3O_4@C/RGO (Fig. 5c and d). RGO can prevent the agglomeration of Fe_3O_4 which enhances the magnetic domain order with better magnetic performance. Fig. S5† shows the dielectric loss tangent ($t_g\delta\varepsilon = \varepsilon''/\varepsilon'$) and magnetic loss tangent ($t_g\delta\mu = \mu''/\mu'$) for Fe_3O_4@C and Fe_3O_4@C/RGO composites. The values of $t_g\delta\varepsilon$ and $t_g\delta\mu$ for Fe_3O_4@C/RGO are larger than those for Fe_3O_4@C, which can be attributed to the addition of RGO. RGO can increase the conductivity of composites and prevent the agglomeration of Fe_3O_4@C, resulting in enhanced microwave absorption abilities. Oxygenic functional groups residing on the surface of RGO can also generate dielectric loss.[37]

The Debye dielectric relaxation model was adopted to investigate the mechanisms of the permittivity dispersion. According to Debye theory, the relationship between ε' and ε'' can be described as:[38]

$$\left(\varepsilon' - \frac{\varepsilon_s - \varepsilon_\infty}{2}\right)^2 + (\varepsilon'')^2 = \left(\frac{\varepsilon_s - \varepsilon_\infty}{2}\right)^2 \quad (3)$$

in which, ε_s and ε_∞ are static permittivity and relative dielectric permittivity at the high frequency limit, respectively. The curve of ε' and ε'' would be a semicircle representing a Debye relaxation process. Fig. S6† shows the ε'–ε'' curves of Fe_3O_4@C and Fe_3O_4@C/RGO composite. It is clearly seen that Fe_3O_4@C/RGO composites have more than two semicircles, whereas Fe_3O_4@C

Table 1 Typical Fe_3O_4-based composites for microwave absorption reported in recentliterature

Filler	Fill loading	Optimum frequency (GHz)	Optimum thickness (mm)	Maximum R_L (dB)	Absorption bandwidth (GHz) (R_L < 10)	Ref.
Carbon@Fe@Fe_3O_4	50%	—	1.5	−40	5.2	[42] (2015)
Fe_3O_4/SiO_2/polyvinylidene fluoride	40%	8.1	2.5	−28.6	—	[43] (2015)
Polyvinylidene fluoride/ Fe_3O_4@polypyrrole	—	16.8	2.5	−21.5	6.1	[44] (2016)
Fe_3O_4@SnO_2/RGO	50%	6.4	4.5	−45.5	3	[45] (2016)
Fe_3O_4/C	60%	3.44	6.2	−55.68	9.55 (R_L < 20)	[46] (2016)
Fe_3O_4/graphene capsules	30%	8.76	3.5	−32	11.6	[47] (2016)
Fe_3O_4@$BaTiO_3$/RGO	50%	5	4	−38.2	13.9	[48] (2016)
Fe_3O_4/polypyrrole/carbon nanotube	20%	10.2	3	−25.9	4.5	[49] (2016)
Fe_3O_4@MnO_2	20%	5.7	4	−42.6	6.7	[50] (2017)
Fe_3O_4@C/RGO	40%	13.9	3	−48.6	7.1	This work

Open Access Article. Published on 24 April 2018. Downloaded on 12/19/2024 5:44:11 AM.
This article is licensed under a Creative Commons Attribution-NonCommercial 3.0 Unported Licence.

only has one, indicating more relaxation processes are generated as a result of the addition of RGO. In the composites, accumulation of charges at the interfaces and the generation of dipoles on particles can cause interfacial polarization.[39] The attenuation constant (α) is widely used to demonstrate the dielectric loss ability of microwave absorbers, which can be expressed by[40]

$$\alpha = \frac{\sqrt{2}\pi f}{c} \times \sqrt{(\mu''_r\varepsilon''_r - \mu'_r\varepsilon'_r) + \sqrt{(\mu''_r\varepsilon''_r - \mu'_r\varepsilon'_r)^2 + (\mu'_r\varepsilon''_r + \mu''_r\varepsilon'_r)^2}}. \quad (4)$$

As shown in Fig. 6a, the α values increase with the increase in composition of RGO, indicating that a high weight ratio of RGO can generate a higher energy attenuation. However, a high dielectric constant also allows for more microwave reflection. Therefore, matching of characteristic impedance is another important factor for microwave absorption materials. According to the principle of impedance matching, when the impedance of incident (Z_{in}) is equal to the impedance of freedom space (Z_0), there is no reflection on the interfaces between the materials and air because of optimal impedance matching with the free space. Therefore, the closer the value of $|Z_{in}/Z_0|$ is to 1, the better the impedance matching. Fig. 6b shows the value of $|Z_{in}/Z_0|$ for Fe_3O_4@C/RGO for different weight ratio of RGO, and indicates that CFG2 and CFG3 have better impedance matching than CFG1 and CFG4. As a result, more RGO can enhance the energy attenuation, however, it will deteriorate the impedance matching which degrades the microwave absorption performance.

In order to evaluate the microwave absorption properties of Fe_3O_4@C and Fe_3O_4@C/RGO composites, the reflection losses (R_L) were calculated. As shown in Fig. S7,† the R_L values of Fe_3O_4@C composite cannot reach −10 dB within the thickness range of 0.5–5.5 mm, and the maximum R_L is −5.5 dB at 18 GHz when the thickness is 5.5 mm, revealing poor microwave absorption ability. However, with the addition of RGO, the R_L of Fe_3O_4@C/RGO composites show significant enhancement. Fig. 7 displays the relationship between R_L, frequency, and thickness for Fe_3O_4@C/RGO composites. It can be seen that the microwave absorption properties of the composites show strong dependence upon the weight ratio of RGO. For CFG1 (Fig. 7a), the maximum value of R_L is −30.1 dB at 8.0 GHz. When the concentration of GO reaches 0.4 mg ml^{-1} (Fig. 7b), a maximum R_L value of −48.6 dB is obtained at 13.9 GHz with a thickness of 3.0 mm, and the absorption bandwidth with the R_L below −10 dB is 7.1 GHz from 10.9 GHz to 18 GHz. Following increase of the concentration of GO to 0.8 mg ml^{-1} and 1.2 mg ml^{-1}, the maximum R_L of CFG3 (Fig. 7c) and CFG4 (Fig. 7d) decrease to −30.4 dB and −15.1 dB, respectively. It is well known that too high a permittivity can result in the strong reflection of microwaves due to harmful impedance matching.[24] The maximum R_L, corresponding absorption bandwidth, and optimum thickness are shown in Table S1.† It is clearly seen that when increasing the content of RGO, the optimum thickness of composite shifts to a low thickness.

Table 1 presents typical Fe_3O_4-based composites and their corresponding microwave absorption properties, from recently published works. Compared with most of them, the Fe_3O_4@C/RGO composites show prominent microwave absorption properties and are attractive candidates for microwave absorbers. In this present Fe_3O_4@C/RGO system, that the Fe_3O_4@C nanorods with porous structure enhanced the microwave absorption properties can be attributed to the following reasons. Firstly, the porous structure can cause multiple reflections which would enhance the absorption of microwaves.[41] Secondly, RGO can be uses as substrate for the deposition of Fe_3O_4@C to prevent their agglomeration, enhancing the contact area between Fe_3O_4@C and microwaves. Thirdly, the residual oxygen functional groups on the RGO surface act as polarized centers which improve reflection loss.[24] Meanwhile, RGO can enhance the impedance matching of composites due to its improved permittivity.

4. Conclusion

In conclusion, porous Fe_3O_4@C core/shell nanorods decorated with reduced graphene oxide were synthesized by a facile one-pot method. The microwave absorption properties of Fe_3O_4@C/RGO composites with different weight ratios of RGO were investigated. The weight ratio of RGO has a significant influence on the microwave absorption properties of Fe_3O_4@C/RGO. When the concentration of GO is 0.4 mg ml^{-1}, the Fe_3O_4@C/RGO composite exhibits excellent microwave absorption properties. A maximum R_L value of −48.6 dB can be obtained at 13.9 GHz with a thickness of 3.0 mm, and the absorption bandwidth with R_L below −10 dB is 7.1 GHz from 10.9 GHz to 18 GHz. The enhanced microwave absorption performance of these composites is mainly attributed to enhanced permittivity, improved impedance matching, the relative dispersing of Fe_3O_4@C compared with pure Fe_3O_4@C, and the residual functional groups on the reduced graphene oxide surface. It is believed that such composites will find widespread applications in the microwave absorption field.

Conflicts of interest

There are no conflicts to declare.

Acknowledgements

This work was supported by the National Basic Research Program: (2016YFA0202300, 2016YFA0202302), the National Natural Science Fund Project under Contract no. (61527817, 61335006, 61378073) and the Beijing Science and Technology Committee (Z151100003315006).

References

1 X. L. Dong, X. F. Zhang, H. Huang and F. Zuo, *Appl. Phys. Lett.*, 2008, **92**, 013127.

 This journal is © The Royal Society of Chemistry 2018

Open Access Article. Published on 24 April 2018. Downloaded on 12/19/2024 5:44:11 AM.
This article is licensed under a Creative Commons Attribution-NonCommercial 3.0 Unported Licence.

2 X. Bai, Y. Zhai and Y. Zhang, *J. Phys. Chem. C*, 2011, **115**, 11673–11677.
3 V. K. Singh, A. Shukla, M. K. Patra, L. Saini, R. K. Jani, S. R. Vadera and N. Kumar, *Carbon*, 2012, **50**, 2202–2208.
4 K. Singh, A. Ohlan, V. H. Pham, R. Balasubramaniyan, S. Varshney, J. Jang, S. H. Hur, W. M. Choi, M. Kumar, S. K. Dhawan, B. S. Kong and J. S. Chung, *Nanoscale*, 2013, **5**, 2411–2420.
5 J. Huo, L. Wang and H. Yu, *J. Mater. Sci.*, 2009, **44**, 3917–3927.
6 J. Shen, Y. Yao, Y. Liu and J. Leng, *J. Mater. Chem. C*, 2016, **4**, 7614–7621.
7 Q. Liu, Q. Cao, H. Bi, C. Liang, K. Yuan, W. She, Y. Yang and R. Che, *Adv. Mater.*, 2016, **28**, 486–490.
8 B. Zhao, B. Fan, Y. Xu, G. Shao, X. Wang, W. Zhao and R. Zhang, *ACS Appl. Mater. Interfaces*, 2015, **7**, 26217–26225.
9 G. Li, T. Xie, S. Yang, J. Jin and J. Jiang, *J. Phys. Chem. C*, 2012, **116**, 9196–9201.
10 X.-J. Zhang, G.-S. Wang, Y.-Z. Wei, L. Guo and M.-S. Cao, *J. Mater. Chem. A*, 2013, **1**, 12115.
11 G. Wang, Z. Gao, G. Wan, S. Lin, P. Yang and Y. Qin, *Nano Res.*, 2014, **7**, 704–716.
12 C. Hu, Z. Mou, G. Lu, N. Chen, Z. Dong, M. Hu and L. Qu, *Phys. Chem. Chem. Phys.*, 2013, **15**, 13038–13043.
13 P. Liu, Y. Huang and X. Zhang, *J. Alloys Compd.*, 2014, **596**, 25–31.
14 J. Zheng, H. Lv, X. Lin, G. Ji, X. Li and Y. Du, *J. Alloys Compd.*, 2014, **589**, 174–181.
15 C. Zhou, S. Geng, X. Xu, T. Wang, L. Zhang, X. Tian, F. Yang, H. Yang and Y. Li, *Carbon*, 2016, **108**, 234–241.
16 D. Sun, Q. Zou, Y. Wang, Y. Wang, W. Jiang and F. Li, *Nanoscale*, 2014, **6**, 6557–6562.
17 H.-L. Xu, H. Bi and R.-B. Yang, *J. Appl. Phys.*, 2012, **111**, 07A522.
18 B. Qu, C. Zhu, C. Li, X. Zhang and Y. Chen, *ACS Appl. Mater. Interfaces*, 2016, **8**, 3730–3735.
19 Y. Ren, C. Zhu, S. Zhang, C. Li, Y. Chen, P. Gao, P. Yang and Q. Ouyang, *Nanoscale*, 2013, **5**, 12296–12303.
20 N. Zhang, Y. Huang and M. Wang, *Composites, Part B*, 2018, **136**, 135–142.
21 Y. Liu, Y. Li, K. Jiang, G. Tong, T. Lv and W. Wu, *J. Mater. Chem. C*, 2016, **4**, 7316–7323.
22 G. Sun, B. Dong, M. Cao, B. Wei and C. Hu, *Chem. Mater.*, 2011, **23**, 1587–1593.
23 Y. Du, W. Liu, R. Qiang, Y. Wang, X. Han, J. Ma and P. Xu, *ACS Appl. Mater. Interfaces*, 2014, **6**, 12997–13006.
24 C. Wang, X. Han, P. Xu, X. Zhang, Y. Du, S. Hu, J. Wang and X. Wang, *Appl. Phys. Lett.*, 2011, **98**, 072906.
25 C. Song, X. Yin, M. Han, X. Li, Z. Hou, L. Zhang and L. Cheng, *Carbon*, 2017, **116**, 50–58.
26 M. Han, X. Yin, L. Kong, M. Li, W. Duan, L. Zhang and L. Cheng, *J. Mater. Chem. A*, 2014, **2**, 16403–16409.
27 M. Zong, Y. Huang, Y. Zhao, L. Wang, P. Liu, Y. Wang and Q. Wang, *Mater. Lett.*, 2013, **106**, 22–25.
28 G.-S. Wang, Y. Wu, Y.-Z. Wei, X.-J. Zhang, Y. Li, L.-D. Li, B. Wen, P.-G. Yin, L. Guo and M.-S. Cao, *ChemPlusChem*, 2014, **79**, 375–381.
29 T. K. Gupta, B. P. Singh, V. N. Singh, S. Teotia, A. P. Singh, I. Elizabeth, S. R. Dhakate, S. K. Dhawan and R. B. Mathur, *J. Mater. Chem. A*, 2014, **2**, 4256.
30 F. Yan, D. Guo, S. Zhang, C. Li, C. Zhu, X. Zhang and Y. Chen, *Nanoscale*, 2018, **10**, 2697–2703.
31 H. Yu, T. Wang, B. Wen, M. Lu, Z. Xu, C. Zhu, Y. Chen, X. Xue, C. Sun and M. Cao, *J. Mater. Chem.*, 2012, **22**, 21679.
32 B. Liang, S. Wang, D. Kuang, L. Hou, B. Yu, L. Lin, L. Deng, H. Huang and J. He, *Nanotechnology*, 2018, **29**, 085604.
33 X. Zheng, W. Lv, Y. Tao, J. Shao, C. Zhang, D. Liu, J. Luo, D.-W. Wang and Q.-H. Yang, *Chem. Mater.*, 2014, **26**, 6896–6903.
34 W. Feng, Y. Wang, J. Chen, L. Wang, L. Guo, J. Ouyang, D. Jia and Y. Zhou, *Carbon*, 2016, **108**, 52–60.
35 H. Xu, M. Shao, T. Chen, S. Zhuo, C. Wen and M. Peng, *Microporous Mesoporous Mater.*, 2012, **153**, 35–40.
36 S. Mondal, U. Rana and S. Malik, *J. Phys. Chem. C*, 2017, **121**, 7573–7583.
37 B. Wen, M. Cao, M. Lu, W. Cao, H. Shi, J. Liu, X. Wang, H. Jin, X. Fang, W. Wang and J. Yuan, *Adv. Mater.*, 2014, **26**, 3484–3489.
38 M. Zong, Y. Huang, Y. Zhao, X. Sun, C. Qu, D. Luo and J. Zheng, *RSC Adv.*, 2013, **3**, 23638.
39 S. He, G.-S. Wang, C. Lu, J. Liu, B. Wen, H. Liu, L. Guo and M.-S. Cao, *J. Mater. Chem. A*, 2013, **1**, 4685.
40 J. N. Ma, X. M. Zhang, W. Liu and G. B. Ji, *J. Mater. Chem. C*, 2016, **4**, 11419–11426.
41 Z. Wang, L. Zhao, P. Wang, L. Guo and J. Yu, *J. Alloys Compd.*, 2016, **687**, 541–547.
42 H. Lv, G. Ji, W. Liu, H. Zhang and Y. Du, *J. Mater. Chem. C*, 2015, **3**, 10232–10241.
43 X. Liu, Y. Chen, X. Cui, M. Zeng, R. Yu and G.-S. Wang, *J. Mater. Chem. A*, 2015, **3**, 12197–12204.
44 Y. Li, Y. Zhao, X. Lu, Y. Zhu and L. Jiang, *Nano Res.*, 2016, **9**, 2034–2045.
45 Y. Wang, Z. Peng and W. Jiang, *Ceram. Int.*, 2016, DOI: 10.1016/j.ceramint.2016.03.180.
46 T. Wu, Y. Liu, X. Zeng, T. Cui, Y. Zhao, Y. Li and G. Tong, *ACS Appl. Mater. Interfaces*, 2016, **8**, 7370–7380.
47 X. Jian, B. Wu, Y. Wei, S. X. Dou, X. Wang, W. He and N. Mahmood, *ACS Appl. Mater. Interfaces*, 2016, **8**, 6101–6109.
48 Z. Peng, W. Jiang, Y. Wang and S. Zhong, *J. Mater. Sci.: Mater. Electron.*, 2015, **27**, 1304–1313.
49 R.-B. Yang, P. M. Reddy, C.-J. Chang, P.-A. Chen, J.-K. Chen and C.-C. Chang, *Chem. Eng. J.*, 2016, **285**, 497–507.
50 M. Qiao, X. Lei, Y. Ma, L. Tian, W. Wang, K. Su and Q. Zhang, *J. Alloys Compd.*, 2017, **693**, 432–439.